Revealing the Impact of Space-Charge Layers on the Li-Ion Transport in All-Solid-State Batteries

Cheng, Zhu; Liu, Ming; Ganapathy, Swapna; Li, Zhaolong; Zhang, Xiaoyu; He, Ping; Zhou, Haoshen; Wagemaker, Marnix; Li, Chau

DOI
10.1016/j.joule.2020.04.002

Publication date
2020

Document Version
Accepted author manuscript

Published in
Joule

Citation (APA)
Cheng, Z., Liu, M., Ganapathy, S., Li, Z., Zhang, X., He, P., Zhou, H., Wagemaker, M., & Li, C. (2020). Revealing the Impact of Space-Charge Layers on the Li-Ion Transport in All-Solid-State Batteries. *Joule*, *4*(6), 1311-1323. https://doi.org/10.1016/j.joule.2020.04.002

Revealing the Impact of Space-Charge Layers on the Li-ion Transport in All-Solid-State Batteries

Zhu Cheng,[1] Ming Liu,[2] Swapna Ganapathy,[2] Chao Li,[1] Zhaolong Li,[2] Xiaoyu Zhang,[1] Ping He,[1*] Haoshen Zhou,[1,3*] and Marnix Wagemaker[2,4*]

[1]Center of Energy Storage Materials & Technology, College of Engineering and Applied Sciences, Jiangsu Key Laboratory of Artificial Functional Materials, National Laboratory of Solid State Microstructures, Collaborative Innovation Center of Advanced Microstructures, Nanjing University, Nanjing 210093, China

[2]Section Storage of Electrochemical Energy, Radiation Science and Technology, Faculty of Applied Sciences, Delft University of Technology, Delft 2629 JB, The Netherlands

[3]Energy Technology Research Institute, National Institute of Advanced Industrial Science and Technology (AIST), 1-1-1, Umezono, Tsukuba 305-8568, Japan

[4]Lead Contact

[*]Correspondence:

pinghe@nju.edu.cn(P.H.)

hszhou@nju.edu.cn(H.Z.)

m.wagemaker@tudelft.nl(M.W.)

Summary

The influence of space-charge layers on the ionic charge transport over cathode-solid electrolyte interface in all-solid-state batteries remains unclear because of the difficulty to unravel it from other contributions to the ion transport over the interfaces. Here we reveal the impact of the space-charge layers by systematically tuning the space-charge layer on and off between $Li_xV_2O_5$ and $Li_{1.5}Al_{0.5}Ge_{1.5}(PO_3)_4$ (LAGP) by changing the $Li_xV_2O_5$ potential and selectively measuring the ion transport over the interface by 2D NMR exchange. The activation energy is demonstrated to be 0.315 eV for lithium-ion exchange over the space-charge free interface, which increases dramatically to 0.515 eV for the interface with a space-charge layer. Comparison with a space-charge model indicates that specifically the charge distribution due to the space-charge layer is responsible for the increased interface resistance. Thereby, the present work provides first quantitative insight in the impact of space-charge layers over electrode-electrolyte interfaces on ionic transport.

Keywords

solid-state batteries, space-charge layers, LAGP, $Li_xV_2O_5$, 2D exchange NMR

Introduction

Lithium batteries are gaining ever increasing attention due to the huge demand for high-energy-density and high-safety electrical energy storage/conversion devices[1–3]. However, commercial lithium-ion batteries suffer from severe safety problems associated with the flammable liquid electrolytes[4,5]. All-solid-state batteries (ASSBs) are considered to be an effective solution to these concerns[6], and in addition to being safer ASSBs also possess additional advantages such as higher practical energy densities and less stringent packaging demands[7]. Although massive research efforts were invested in ASSBs over the last years, facile lithium-ion transport within the ASSBs remains a grand challenge, standing in the way towards market application of ASSBs[8–10]. Over the last few years a number of solid-state electrolytes have been discovered with unexpectedly high ionic conductivities in the range of 10^{-3}~10^{-2} S cm^{-1}, which makes that the bulk ionic conductivity of solid-state electrolytes is no long a major concern[11–13]. Currently, the solid-solid interface between the electrode and solid-state electrolyte presents the largest challenges. Firstly, the small effective interface area between the solid electrolyte and electrode can lead to a large barrier for charge transfer. Secondly, ion transport may be challenged by electrochemical decomposition reactions of the solid electrolyte in combination with the electrode, leading to poorly Li-ion conducting interphases[14,15]. Thirdly, the volumetric changes associated with the decomposition reactions, as well as the reversible ion storage in the electrodes, can lead to contact loss[16,17]. Finally, the space-charge layer, the formation of electrochemical double layers at the solid-solid electrode-electrolyte interfaces typically results in local charge carrier depletion/enrichment, which in turn may influence the charge transport[15,18–20]. The space-charge layer can enhance the ionic condition in solid-solid dispersions having intrinsic poor bulk ionic conductivity[21–24], but for solid electrolytes that are designed to have a high conductivity it is expected to be detrimental for ion transport by creating an interface barrier for Li-ion transport[25,26]. However, the impact of space-charges on the charge transport is very unclear, as demonstrated by the very different results reported[27–29] which can mainly be ascribed to the difficulty to observe the lithium-ion distributions at the interfaces on the atomic scale and the many material aspects as well as electrochemical conditions that influence the interface properties.

The present work aims at quantifying and understanding the impact of space-charge layers on the lithium-ion migration across the solid-solid cathode-electrolyte interface by systematically varying the space charge through controlling the Li-chemical potential of the electrode material. Specifically the LAGP-$Li_xV_2O_5$ interface is investigated where the chemical potential of Li in the $Li_xV_2O_5$[30–32] electrode can be controlled by the composition between 2 and 4 V vs Li/Li^+ by means of the solid solution reaction, rationalizing the selection of the active material. Specifically, the LiV_2O_5, $Li_2V_2O_5$ and $Li_{0.2}V_2O_5$ compositions are prepared by chemical lithiation, having the same, a lower and a higher Li chemical potential, respectively, as compared to that in

LAGP. In this way the space-charge layer at the LAGP-$Li_xV_2O_5$ interface will be switched off for LiV_2O_5 and switched on for $Li_{0.2}V_2O_5$ and $Li_2V_2O_5$, albeit with reversed polarity. As the potential range of $Li_xV_2O_5$ falls within the expected electrochemical stability of LAGP[33], a stable interface between LAGP and $Li_xV_2O_5$ is expected, thereby exposing the impact of the space-charge layer. To measure the Li-ion equilibrium transport over these interfaces, we employed two-dimension exchange NMR spectroscopy (2D-EXSY), a powerful method to investigate the Li-ion transport over the interfaces[34–36]. These experiments show that switching on the space-charge layer leads to a significant increase in the activation energy for Li-ion diffusion over the LAGP-$Li_2V_2O_5$ interface, in agreement with a 4-fold increase in resistance calculated with space-chare layer model. Thereby, direct evidence of the impact of space-charge layer on the Li-ion transport over the solid electrolyte–electrode interfaces is provided, which demonstrates that it can contribute significantly to the internal resistance. These insights motivate to develop rational interface strategies to reduce the space-charge layer effect in ASSBs in order to improve the ASSBs performance, for instance through reducing the local chemical potential differences at the electrode-electrolyte interfaces.

Results and Discussion

Equilibrium potential of LAGP and $Li_xV_2O_5$

The diffraction peaks of the prepared LAGP material in Figure S1A can be indexed with the NASICON $LiGe_2(PO_4)_3$ structure, indicating the successful synthesis of LAGP. The crystallite size from X-ray diffraction (XRD) line broadening results in an average LAGP particle size of 110 nm. The LAGP pellet was coated with Au on both sides for the impedance measurements. From the fitting result of Figure S1B, the calculated ionic conductivity of the as prepared LAGP is 0.12 mS cm^{-1} consistent with previously reported values[37], demonstrating the high ionic conductivity. Although LAGP is considered to be a quite stable solid-state electrolyte, a small amount lithium can still be extracted from its crystal structure by electrochemical charging at small current densities[38]. The LAGP powder is used as cathode to assemble a LAGP/Li cell of which the galvanostatic intermittent titration technique (GITT) measurement, repeatedly 30 minutes charging at 5 $\mu A\cdot cm^{-1}$ and 8 h resting, is shown in Figure 1A. The cut-off voltage of this GITT measurement is set to 4.6 V to avoid electrolyte decomposition at higher potentials. After the first charging and rest step, the voltage of LAGP/Li cell returns to 3 V as demonstrated in Figure 1A, which implies that the equilibrium potential of LAGP is around 3 V (the extracted lithium content in the first charging process is negligible considering a small current density of 5 $\mu A\ cm^{-1}$). GITT measurements were also conducted on the V_2O_5/Li cells to determine the relationship between the composition and the equilibrium potential. In figure 1B, the GITT curve shows the typical $Li_xV_2O_5$ electrochemical behaviour with a gradual decreasing voltage between 3.6 and 2.4 V vs Li/Li^+, representing a solid solution reaction, and a plateau around 2.4 V, representing a first order phase transition[39]. This demonstrates that the equilibrium potential of $Li_xV_2O_5$ can be adjusted between 2.4 V to 3.6 V by tuning the composition between $0 < x < 2$. The GITT indicates that LiV_2O_5 has the same equilibrium potential as LAGP, comparing figure 1A and 1B, which was achieved by discharging the V_2O_5

at 0.05 C for 10 h followed by a rest of 100 h, as shown in Figure 1D. This means that when LiV_2O_5 and LAGP are mixed together, there is no difference in Li-chemical potential, and hence there is no driving force to establish a space-charge layer. To establish a difference in Li-chemical potential, V_2O_5 was discharged at 0.05 C to equilibrium potentials of 3.4 and 2.4 V vs Li/Li^+ corresponding to $Li_{0.2}V_2O_5$ and $Li_2V_2O_5$ respectively, as shown in Figure 1C and 1E. The potential difference, or equivalent the difference in Li chemical potential, at the $Li_{0.2}V_2O_5$-LAGP interface (0.4 V) and $Li_2V_2O_5$-LAGP interface (0.6 V) will lead to the redistribution of Li-ions to equalize the electrochemical potential over the interface, hence establishing a space-charge layer.

Li-ion kinetics in bulk $Li_{0.2}V_2O_5$, LiV_2O_5 and $Li_2V_2O_5$

To prepare larger amounts of carbon black and binder free $Li_xV_2O_5$ materials, as required for the detailed solid-state NMR studies, chemical lithiation was employed. ICP analysis of the prepared LiV_2O_5, $Li_2V_2O_5$ and $Li_{0.2}V_2O_5$ materials results in the expected lithium content, as can be seen in Table S1. The XRD refinements, see Figure S2, show an increase in the c parameter with increased lithium content in $Li_xV_2O_5$, indicating the puckering of the V_2O_5 layer[40]. To identify the Li-ion environment and kinetics in $Li_xV_2O_5$, one dimensional (1D) ^{6}Li NMR was performed, the spectra of which are shown in Figure 2A-2C. As shown in Figure 2A and 2B, there are four different lithium environments appearing at ~11 ppm, 0.6 ppm, -0.3 ppm and -8 ppm. Based on previous neutron diffraction and ^{7}Li MAS (magic angle spinning) NMR results[41], the resonance around 11 ppm represents Li occupying the octahedral site, which is expected for $x<1$ in $Li_xV_2O_5$, consistent with the decreased peak intensity at ~11 ppm in $Li_2V_2O_5$ compared with LiV_2O_5. The resonance located at -8 ppm is assigned to the ε/δ-phase in LiV_2O_5 and $Li_2V_2O_5$ as reported previously[42,43]. The other two resonances located near 0 ppm have been suggested to represent the Li-environment in the γ-phase in LiV_2O_5 and $Li_2V_2O_5$, while other studies suggest that only one resonance near 0 ppm corresponds to the γ-phase[42,44,45]. A possible explanation is that previous NMR studies of $Li_xV_2O_5$ were conducted using ^{7}Li (I=3/2) NMR, having a lower resolution due to quadrupolar interactions, resulting in two resonances overlapping as demonstrated in the ^{7}Li NMR MAS spectrum of LiV_2O_5 and $Li_2V_2O_5$ shown in Figure S3. In $Li_{0.2}V_2O_5$ there is only one broad resonance located around -24 ppm corresponding to the β-phase in low lithium content $Li_xV_2O_5$[42]。

To determine the lithium-ion bulk diffusion kinetics of the compositions LiV_2O_5, $Li_2V_2O_5$ and $Li_{0.2}V_2O_5$, spin-spin (T_2) relaxation NMR experiments were carried out at temperatures ranging from 258 K to 438 K. In the analysis of the T_2 relaxation of LiV_2O_5 and $Li_2V_2O_5$ only the peak at -0.3 ppm was fitted as only this lithium-ion environment appears to contribute to the Li-ion conductivity as discussed below. As can be seen in Figure 2D-2F, for all compositions the spin-spin relaxation rate, $1/T_2$, remains constant until a specific temperature above which it increases with increasing temperature. The T_2 value at the "freezing" temperature range is related to the correlation time τ_c which is the lower limit of the average time for a Li ion residing at one site before it hops to another site at that temperature.[46] The Bloembergen, Purcell, and Pound (BPP) model was applied to fit the spin-spin relaxation as described in supporting information. Figure 2D-2F represents the Arrhenius plots for LiV_2O_5, $Li_2V_2O_5$ and $Li_{0.2}V_2O_5$ resulting in activation energies of $0.17 \pm\ 0.02$ eV, $0.08 \pm\ 0.01$ eV and $0.13 \pm\ 0.01$ eV for lithium-ion in LiV_2O_5, $Li_2V_2O_5$ and $Li_{0.2}V_2O_5$ respectively. The correlation times calculated via $\tau_c = T_2/\sqrt{2}$ from the break point between the low and mobility regime indicated by the crossing lines in Figure 2D-2F are 12.4 μs at ~360 K for LiV_2O_5, 11.4 μs at ~373 K for $Li_2V_2O_5$ and 27.1 μs at ~317 K for $Li_{0.2}V_2O_5$. With these values, τ_∞ is computed to be 52 ns, 950 ns and 230 ns which leads to τ_c of 38.6 μs, 21.3 μs and 36.2 μs at room temperature for LiV_2O_5, $Li_2V_2O_5$ and $Li_{0.2}V_2O_5$ respectively. The microscopic diffusion coefficient at room temperature is usually determined with $\mathrm{D} = l^2/n\tau_c$, where l is the length of an elementary jump between sites and n is the dimension factor. Assuming in LiV_2O_5 the Li^+ jump occurs along channels parallel to the b-axis ([0 1 0] direction) , so the Li^+ can jump from the octahedral site to other two equivalent sites representing 1-D diffusion, which leads to $\mathrm{n} = 2$ and the jump distance is equal to the b-lattice parameter[42,47]. As a result, we could obtain 1.68×10^{-11} $cm^2\ s^{-1}$, 3.04×10^{-11} $cm^2\ s^{-1}$ and 1.79×10^{-11} $cm^2\ s^{-1}$ for the diffusion coefficient at room temperature for LiV_2O_5, $Li_2V_2O_5$ and $Li_{0.2}V_2O_5$ individually. These very similar diffusion coefficients indicate that the bulk ion conductivity in these three phases is comparable.

Influence of space-charge layers on the Li-ion transport

To investigate the Li-ion transport over the interfaces between $Li_xV_2O_5$ and LAGP, mixtures are prepared by hand grinding ballmilled $Li_xV_2O_5$ and LAGP powders, followed by pressing this mixture into a pellet under 100 MPa to establish the contact between $Li_xV_2O_5$ and LAGP, representing the conditions in actual solid-state batteries. After this the pellet was hand grinded in a mortar to enable filling the NMR rotor. Prior to the NMR experiments the stability of the mixtures is investigated by conducting XRD and X-ray photoelectron spectroscopy (XPS) measurements. As observed in Figure S4 and S5, the results show no indication that $Li_xV_2O_5$ and LAGP react with each other, in line with the expected electrochemical stability window of LAGP[33] towards the potentials of the $Li_xV_2O_5$ x=0.2-2 compositions.

1D ^{6}Li MAS NMR spectra of LiV_2O_5-LAGP, $Li_2V_2O_5$-LAGP and $Li_{0.2}V_2O_5$-LAGP mixtures are displayed in Figure 3A, 3E and 3I. In all three mixtures, the weight ratio between $Li_xV_2O_5$ and LAGP was set to 4:1. In Figure 3A and 3E the two overlapping resonances around 0 ppm represent Li in LiV_2O_5 and $Li_2V_2O_5$ and the sharp resonance around -1.4 ppm represents the lithium environment in LAGP. Note that the two additional broad resonances of LiV_2O_5 and $Li_2V_2O_5$, visible in Figure 2A and 2B practically fade into the background due to their relative low intensity as shown in Figure S6. As expected, based on Figure 2C the $Li_{0.2}V_2O_5$-LAGP mixture shown in Figure 3I results in the broad resonance of $Li_{0.2}V_2O_5$ at -24 ppm in addition to the sharp LAGP resonance at -1.4 ppm.

To investigate the impact of the presence of space-charge layers on the lithium-ion transport kinetics over the $Li_xV_2O_5$-LAGP interfaces, 2D exchange NMR measurements were conducted for the LiV_2O_5-LAGP, $Li_2V_2O_5$-LAGP and $Li_{0.2}V_2O_5$-LAGP mixtures. 2D exchange NMR offers the possibility to measure the spontaneous lithium-ion exchange between different lithium-ion environments, at present for the first time realized to study the impact of the space-charge layers between two solid phases. 2D exchange NMR effectively records the spectrum of the ^{6}Li atoms at t = 0 s , allows a "mixing time" t_{mix}, subsequently recording the spectrum of the same ^{6}Li atoms again at $t = t_{mix}$. The results of these measurements are shown in Figure 3. The signal appearing on the diagonal reflects the 1D NMR signal in Figure 3A, 3E and 3I, which represents ^{6}Li atoms having the same environment before and after t_{mix}. In contrast, the off-diagonal signal represents ^{6}Li atoms that have exchanged between the $Li_xV_2O_5$ and LAGP environments within the diffusion time t_{mix}. For a short mixing time of 0.5 ms (Figure 3B and 3F), there is virtually no lithium-ion exchange and thus not sufficient Li-ions crossing the $Li_xV_2O_5$-LAGP interface to be measured by the exchange experiments. For a much longer mixing time, t_{mix}=1 s, clear cross-peaks appear in the 2D exchange spectrum of both LiV_2O_5-LAGP and $Li_2V_2O_5$-LAGP mixtures. The weaker cross-peaks intensity for the $Li_2V_2O_5$-LAGP mixture implies significant less lithium-ion exchange as compared to that in LiV_2O_5-LAGP, as shown in Figure 3D and 3H. The stronger cross-peak intensity for the LiV_2O_5-LAGP mixture signifies more facile Li-ion diffusion over the LiV_2O_5-LAGP interface. For the $Li_{0.2}V_2O_5$-LAGP mixture no cross peaks are observed at a long mixing time of t_{mix}=1 s, Figure 3J, even at an elevated temperature of 363 K, Figure 3K, indicating that for this mixture the spontaneous lithium transport between $Li_{0.2}V_2O_5$ and LAGP is the smallest. Note that the two resonances in LiV_2O_5 and $Li_2V_2O_5$ around 11 ppm and -8 ppm are invisible in the 2D exchange spectrum because of the relatively low intensity, as further illustrated by Figure S7. To further investigate the exchange in the $Li_{0.2}V_2O_5$-LAGP mixture, ^{7}Li NMR 2D experiments were conducted, raising the resonance intensities because of the higher natural abundance (^{7}Li 92.4% vs ^{6}Li 7.6%)[48] and the higher NMR sensitivity, however, at the expense of the lower resolution caused by the stronger dipolar interactions and presence of quadrupolar interactions. Despite the higher sensitivity on lithium exchange, even this experiment did not result in measurable exchange, see Figure 3L. As the strongest lithium exchange over the $Li_xV_2O_5$-LAGP interface is observed for the composition where the space-charge layer should be absent, x=1, these results demonstrate that the space-charge layer, expected to be present for the compositions x=0.2 and x=2, hinders the spontaneous lithium exchange.

More detailed evaluation of the 2D spectrum at 363 K brings forward another exchange phenomenon for the $Li_2V_2O_5$-LAGP mixture shown in Figure 4B, which is not present for the LiV_2O_5-LAGP mixture shown in Figure 4A. The off-diagonal intensity indicates exchange between Li-sites within $Li_2V_2O_5$ located at ~0.6 ppm and -0.3 ppm, representing sites within the γ-phase. The different site occupation in $Li_2V_2O_5$ appears to boost the bulk diffusivity, also reflected by the higher diffusion coefficient as compared to LiV_2O_5 resulting from the T_2 relaxation experiments. Despite the higher bulk diffusivity in $Li_2V_2O_5$ the Li-ion exchange over the interface with the LAGP is significantly less as compared to LiV_2O_5, reflecting the large impact of the space-charge layer on the spontaneous Li-ion transport.

To quantify the exchange over the LiV_2O_5-LAGP and $Li_2V_2O_5$-LAGP interfaces, variable temperature ^{6}Li 2D exchange experiments were carried out. Quantification of the exchange between LiV_2O_5 ($Li_2V_2O_5$) and LAGP was performed by fitting the growing off-diagonal signal by a diffusion model derived from Fick's law as described in supporting information. The fitted results of the normalized cross-peaks intensity as a function of mixing time for different temperatures are shown in Figure 5. By means of fitting the above demagnetization model, each temperature results in a diffusion coefficient, quantifying the activation energy for exchange between the $Li_xV_2O_5$ and LAGP phases, the results of which are shown in Figure 5A and 5C.

For the space-charge layer free LiV_2O_5-LAGP interface, the observed Li exchange at room temperature leads to an effective diffusion coefficient of approximately 1.0×10^{-12} cm^2 s^{-1}, see Figure S9, which is a factor of 17 times smaller than the bulk diffusion coefficient as determined by T_2 relaxation. Additionally, the activation energy for diffusion over the interface, 315 meV, is much larger than that for bulk diffusion, amounting 170 meV from the T_2 relaxation experiments in Figure 2D. This most likely indicates that the grain boundary between space-charge free LiV_2O_5-LAGP offers restricted contact points as well as introducing an additional diffusional barriers[36,49], as also suggested by the EIS measurement of the LiV_2O_5-LAGP mixtures in Figure S8, reflecting one of the main challenges to achieve high performance ASSBs.

Driven by the 0.6 V difference in lithium chemical potential, introduction of the space-charge layer at the $Li_2V_2O_5$-LAGP interface increases the resistance of the interface against charge transport significantly. The effective diffusion coefficient drops to 4.4×10^{-14} cm^2 s^{-1} as shown in Figure S9, more than 20 times smaller compared to the space-charge free LiV_2O_5-LAGP interface and the activation energy for exchange raises to 515 meV. The decreased Li-ion exchange must be due to the presence of the space-charge layer because the diffusivity of the bulk LAGP is the same for all three systems, amounting ~10^{-13} cm^2 s^{-1} and 166 meV[50], and because the bulk diffusivity of the three $Li_xV_2O_5$ phases is comparable, as determined by the T_2 relaxation experiments (x=0.2: 1.79×10^{-11} cm^2 s^{-1} , x=1: 1.68×10^{-11} cm^2 s^{-1} and x=2: 3.04×10^{-11} cm^2 s^{-1}). As schematically shown in Figure 5B and 5D, the space-charge layer poses an additional barrier, on top of that posed by the grain boundary, that hinders the Li-ion transport over the electrode-electrolyte interface.

Because the NMR exchange experiments are performed under equilibrium conditions, it provides a direct quantitative measurement of the exchange current density over the electrode-electrolyte interface, thus reflecting the intrinsic mobility of the Li-ions over the interface. During the same mixing time of 1 s at room temperature, about 57% of the total amount of lithium-ions exchanged over the LiV_2O_5-LAGP interface while for $Li_2V_2O_5$-LAGP only 30% lithium-ion exchanged as shown in Figure 5A and 5C. From the amount of the exchanged lithium-ion, and taking into consideration of the average crystallite sizes of $Li_xV_2O_5$ and LAGP, we obtain the room temperature exchange current density which is deemed as one of the critical parameters that will determine the maximum power of a battery, amounting 0.77 mA cm^{-2} for space-charge layer free LiV_2O_5-LAGP and 0.41 mA cm^{-2} in the presence of the space-charge layer in $Li_2V_2O_5$-LAGP. To estimate the maximum exchange current density over the $Li_{0.2}V_2O_5$-LAGP, where no exchange is observed, we assume that the exchange is at most in the order of the background signal resulting in a maximum exchange current density of 0.13 mA cm^{-2} over the $Li_{0.2}V_2O_5$-LAGP interface. The larger exchange current density for LiV_2O_5-LAGP as compared to the $Li_2V_2O_5$-LAGP and $Li_{0.2}V_2O_5$-LAGP interfaces further demonstrates that the space-charge layer hinders the lithium-ion exchange over the interface significantly. For comparison, the exchange current density at typical electrode-liquid electrolyte interfaces in Li-ion batteries exceeds 1 mA cm^{-2} [51,52], underlining that the solid-solid interfaces limit the power density of ASSBs.

To gain more insight in the role of the space-charge layers, the space-charge layer model from our previous work[53] is applied to the $Li_xV_2O_5$-LAGP interfaces. Assuming that only ions are mobile and the interface is chemically stable with perfect contact, by using a solid solution model the chemical potential as a function of the distance near the interface can be determined from the corresponding ion concentration, where the law of mass conservation serves as the boundary condition. Specially the columbic interaction between defects is taken into account, as was proposed by Maier and co-workers[54,55] which is essential to approximate the formation energy of vacancies. This model does not take into account the electron (hole) transfer through band bending at the cathode-solid electrolyte interface, which can have a large impact on the space charge formation, as recently predicted for the LiPON-Li_xCoO_2 by Swift and Qi[56]. Because of the large bandgap of $Li_xV_2O_5$[57] and its position relative to the bandgap to that of LAGP[58], the valence band maxima are far apart, unlike at the LiPON-Li_xCoO_2 interface [59]. As a consequence, it should be expected that band bending has less impact on the space charge formation in the present system, suggesting that the current model is a good approximation for the investigated interfaces. The parameters to perform the space-charge model calculations are listed in Table S2. The voltages of LAGP, LiV_2O_5, $Li_2V_2O_5$, and $Li_{0.2}V_2O_5$ are set to be 3 V, 3 V, 2.4 V and 3.4 V respectively, which is based on the electrochemical measurements in Figure 1. As displayed in Figure 6B and 6C, in $Li_2V_2O_5$-LAGP and $Li_{0.2}V_2O_5$-LAGP the difference in potential between electrode and solid electrolyte, reflects the difference in Li chemical potential, which results in the redistribution of the Li-ion concentration at the interface to equalize the electrochemical potential. This represents the formation of the space-charge layer having a ~0.5 nm thickness for $Li_2V_2O_5$-LAGP and ~0.7 nm for the $Li_{0.2}V_2O_5$-LAGP interface. This indicates that space charges occur over only a few atomic layers adjacent to the interfaces. Only taking the changes in lithium concentration into account, the resistance because of the space-charge layers for $Li_2V_2O_5$-LAGP and $Li_{0.2}V_2O_5$-LAGP are very small, amounting 0.0009 and 0.0061 Ω cm^2 respectively (see Figure S10). It should be noted that the predicted large local depletion in LAGP at the $Li_{0.2}V_2O_5$-LAGP interface may lead to the LAGP structure to collapse at the interfaces, potentially posing an additional barrier for Li-ion transport.

From the measured exchange current density the interface resistance can be determined based on the relationship given by G.Horvai[60]. The resulting interface resistances are approximately 33 Ω cm^2 for space-charge layer free LiV_2O_5-LAGP increasing to 63 Ω cm^2 for $Li_2V_2O_5$-LAGP and 188 Ω cm^2 for $Li_{0.2}V_2O_5$-LAGP. These values are five orders of magnitude larger as compared to that from the space-charge layer calculations. The model calculations only approximately take into account the impact of the composition on the diffusion coefficient, and not the impact of the grain boundary resistance that is anticipated to exist between the electrolyte and electrode particles[49] (see also Figure S8) and also not the charge dipole due to the space-charge layer[56]. Based on this it is concluded that the impact of the changes in Li-ion concentrations in the space-charge layers have a negligible impact on the interface resistance as compared to the grain boundary resistance, and that the charge separation of the space-charge layer is responsible for the significant increase in the interface resistance. For the present electrolyte-electrode combination the space-charge layer is demonstrated to add more than 100 Ω cm^2 to the interface resistance. For LAGP assuming a conductivity of 10^{-3} S cm^{-1}, the corresponding resistance for a 100 μm thick solid electrolyte is 10 Ω cm^2, demonstrating the potentially large contributions of space-charge layers to the internal resistance of ASSBs, depending on the electrode and electrolyte geometry. Clearly, the resistance due to the space charge layer will strongly vary depending on the electrode potential, in the present case depending on the $Li_xV_2O_5$ composition, and thus on the state of charge. Moreover, also the kinetic polarization of the electrode during high rate cycling can be expected to affect the space-charge layer, depending on the detailed resistances towards both Li-ion and electron charge carriers.

Conclusion and outlook

Using $Li_xV_2O_5$-LAGP as model system, the present NMR measurements and model calculations demonstrate the important role of space-charge layers at the cathode-solid electrolyte interface. The lithium-ion transport kinetics from cathode to solid electrolyte (and vice versa) can be directly measured by 2D NMR exchange experiments, a direct probe of the exchange current density. For the LiV_2O_5-LAGP interface, where there is no space-charge layer based on the equal Li chemical potential, the activation energy for Li-exchange and the resistance towards Li-ion transport is found to be significantly smaller than in $Li_2V_2O_5$-LAGP where the difference in Li chemical potential results in a space-charge layer at the interface. Consistently, the exchange current density directly measured by the NMR exchange experiments drops with the presence of the space- charge layer, providing direct insight in the interface resistance posed by the charge distribution as a consequence of the space-charge layer. Thereby, this work reveals the quantitative impact of the space-charge layers at the cathode-solid electrolyte interface in ASSBs, pointing out the importance of strategies to mitigate the space-charge layer effects, for instance by reducing the local chemical potential difference at the cathode-solid electrolyte interface.

Resource Availability

Lead Contact

Further information and requests for resources and materials should be directed to and will be fulfilled by the Lead Contact, Marnix Wagemaker (m.wagemaker@ tudelft.nl).

Materials Availability

The materials generated in this study will be made available on reasonable request.

Data and Code Availability

Supporting data and code of this study will be made available on reasonable request.

Experimental procedures

Full details of all experiments and materials are provided in Supplemental Experimental Procedures.

Acknowledgements

The authors thank Frans Ooms for the assistance with experiments. This research was partially supported by the National Key Research and Development Program of China (2016YFB0100203), the National Natural Science Foundation of China (21922508, 21673116, 21633003, U1801251), the Natural Science Foundation of Jiangsu Province of China (BK20190009), and the PAPD of Jiangsu Higher Education Institutions. The authors acknowledge support by the Netherlands Organization for Scientific Research (NWO) under the grant nr. 15788 and M.W. under the VICI grant nr. 16122. Financial support from the Advanced Dutch Energy Materials (ADEM) program of the Dutch Ministry of Economic Affairs, Agriculture and Innovation is gratefully acknowledged. Financially supporting of the work from the Chinese Scholarship Council (CSC) is gratefully acknowledged.

Author contributions

M.W., H.Z. and P.H. conceived and designed the project. Z.C., S.G. and M.L. performed the NMR experiments. C.L. provided the samples. M.L. helped with the XRD, XPS experiments and Z.L. helped with the XRD refinements. Z.C. and S.G. analysed experiment results, with contributions from X.Z. and P.H. to scientific discussion. Z.C. and M.W wrote the manuscript. Z.C. and M.L. contributed equally to the work. All the authors helped in writing the manuscript.

Declaration of Interests

The authors declare no competing interests.

References

1. Goodenough, J.B., and Park, K.S. (2013). The Li-ion rechargeable battery: A perspective. J. Am. Chem. Soc. *135*, 1167–1176.

2. He, P., Yu, H., Li, D., and Zhou, H. (2012). Layered lithium transition metal oxide cathodes towards high energy lithium-ion batteries. J. Mater. Chem. *22*, 3680–3695.

3. Ganapathy, S., and Wagemaker, M. (2012). Nanosize storage properties in spinel Li4Ti5O12 explained by anisotropic surface lithium insertion. ACS Nano *6*, 8702–8712.

4. Xu, K. (2004). Nonaqueous liquid electrolytes for lithium-based rechargeable batteries. Chem. Rev. *104*, 4303–4417.

5. Liu, X., Peng, S., Gao, S., Cao, Y., You, Q., Zhou, L., Jin, Y., Liu, Z., and Liu, J. (2018). Electric-field-directed parallel alignment architecting 3D lithium-ion pathways within solid composite electrolyte. ACS Appl. Mater. Interfaces *10*, 15691–15696.

6. Lotsch, B. V., and Maier, J. (2017). Relevance of solid electrolytes for lithium-based batteries: A realistic view. J. Electroceramics *38*, 128–141.

7. Takada, K. (2013). Progress and prospective of solid-state lithium batteries. Acta Mater. *61*, 759–770.

8. Wang, C., Xie, H., Zhang, L., Gong, Y., Pastel, G., Dai, J., Liu, B., Wachsman, E.D., and Hu, L. (2018). Universal soldering of lithium and sodium alloys on various substrates for batteries. Adv. Energy Mater. *8*, 1–8.

9. Han, X., Gong, Y., Fu, K., He, X., Hitz, G.T., Dai, J., Pearse, A., Liu, B., Wang, H., Rubloff, G., et al. (2017). Negating interfacial impedance in garnet-based solid-state Li metal batteries. Nat. Mater. *16*, 572–579.

10. Bae, J., Li, Y., Zhang, J., Zhou, X., Zhao, F., Shi, Y., Goodenough, J.B., and Yu, G. (2018). A 3D nanostructured hydrogel-framework-derived high-performance composite polymer lithium-Ion electrolyte. Angew. Chemie - Int. Ed. *57*, 2096–2100.

11. Kamaya, N., Homma, K., Yamakawa, Y., Hirayama, M., Kanno, R., Yonemura, M., Kamiyama, T., Kato, Y., Hama, S., Kawamoto, K., et al. (2011). A lithium superionic conductor. Nat. Mater. *10*, 682–686.

12. Deiseroth, H.J., Kong, S.T., Eckert, H., Vannahme, J., Reiner, C., Zaiß, T., and Schlosser, M. (2008). Li6PS5X: A class of crystalline Li-rich solids with an unusually high Li^+ mobility. Angew. Chemie - Int. Ed. *47*, 755–758.

13. Kim, S., Oguchi, H., Toyama, N., Sato, T., Takagi, S., Otomo, T., Arunkumar,

D., Kuwata, N., Kawamura, J., and Orimo, S. (2019). A complex hydride lithium superionic conductor for high-energy-density all-solid-state lithium metal batteries. Nat. Commun. *10*, 1081.

14. Xu, L., Tang, S., Cheng, Y., Wang, K., Liang, J., Liu, C., Cao, Y.-C., Wei, F., and Mai, L. (2018). Interfaces in solid-state lithium batteries. Joule *2*, 1991-2015.

15. Zhang, Z., Shao, Y., Lotsch, B., Hu, Y.S., Li, H., Janek, J., Nazar, L.F., Nan, C.W., Maier, J., Armand, M., et al. (2018). New horizons for inorganic solid state ion conductors. Energy Environ. Sci. *11*, 1945–1976.

16. Janek, J., and Zeier, W.G. (2016). A solid future for battery development. Nat. Energy *1*, 16141.

17. Yu, X., and Manthiram, A. (2018). Electrode-electrolyte interfaces in lithium-based batteries. Energy Environ. Sci. *11*, 527–543.

18. Takada, K., Ohta, N., Zhang, L., Xu, X., Hang, B.T., Ohnishi, T., Osada, M., and Sasaki, T. (2012). Interfacial phenomena in solid-state lithium battery with sulfide solid electrolyte. Solid State Ionics *225*, 594–597.

19. Takada, K., Ohno, T., Ohta, N., Ohnishi, T., and Tanaka, Y. (2018). Positive and negative aspects of interfaces in solid-state batteries. ACS Energy Lett. *3*, 98–103.

20. Takada, K., Ohta, N., and Tateyama, Y. (2015). Recent progress in interfacial nanoarchitectonics in solid-state batteries. J. Inorg. Organomet. Polym. Mater. *25*, 205–213.

21. Maier, J. (1987). Defect chemistry and conductivity effects in heterogeneous solid electrolytes. J. Electrochem. Soc. *134*, 1524.

22. Maier, J. (1984). Enhancement of the ionic conductivity in solid-solid-dispersions by surface induced defects. Physical Chem. Chem. Phys. *88*, 1057–1062.

23. Maier, J. (2005). Nanoionics: ion transport and electrochemical storage in confined systems. Nat. Mater. *4*, 805–815.

24. Yamada, H., Suzuki, K., Oga, Y., Saruwatari, I., and Moriguchi, I. (2013). Lithium depletion in the solid electrolyte adjacent to cathode materials. ECS Trans. *50*, 1–12.

25. Luntz, A.C., Voss, J., and Reuter, K. (2015). Interfacial challenges in solid-state

Li ion batteries. J. Phys. Chem. Lett. *6*, 4599–4604.

26. Takada, K. (2018). Progress in solid electrolytes toward realizing solid-state lithium batteries. J. Power Sources *394*, 74–85.

27. Goodyer, C.E., Fish, J.S., Fehribach, J.D., O'Hayre, R., and Bunge, A.L. (2011). Modeling space charge layer interaction and conductivity enhancement in nanoionic composites. Electrochim. Acta *56*, 9295–9302.

28. Okumura, T., Nakatsutsumi, T., Ina, T., Orikasa, Y., Arai, H., Fukutsuka, T., Iriyama, Y., Uruga, T., Tanida, H., Uchimoto, Y., et al. (2011). Depth-resolved X-ray absorption spectroscopic study on nanoscale observation of the electrode-solid electrolyte interface for all solid state lithium ion batteries. J. Mater. Chem. *21*, 10051–10060.

29. Brogioli, D., Langer, F., Kun, R., and La Mantia, F. (2019). Space-charge effects at the LLZO/PEO interface. ACS Appl. Mater. Interfaces *11*, 11999-12007.

30. Cocciantelli, J.M., Ménétrier, M., Delmas, C., Doumerc, J.P., Pouchard, M., Broussely, M., and Labat, J. (1995). On the delta to gamma irreversible transformation in Li//V_2O_5 secondary batteries. Solid State Ionics *78*, 143–150.

31. Liu, J., Zhou, Y., Wang, J., Pan, Y., and Xue, D. (2011). Template-free solvothermal synthesis of yolk-shell V_2O_5 microspheres as cathode materials for Li-ion batteries. Chem. Commun. *47*, 10380–10382.

32. Pan, A., Wu, H. Bin, Yu, L., Zhu, T., and Lou, X.W. (2012). Synthesis of hierarchical three-dimensional vanadium oxide microstructures as high-capacity cathode materials for lithium-ion batteries. ACS Appl. Mater. Interfaces *4*, 3874–3879.

33. Xu, X., Wen, Z., Wu, X., Yang, X., and Gu, Z. (2007). Lithium ion-conducting glass-ceramics of Li1.5Al0.5Ge1.5(PO4)3-xLi2O (x=0.0-0.20) with good electrical and electrochemical properties. J. Am. Ceram. Soc. *90*, 2802–2806.

34. Wagemaker, M., Kentjens, A.P.M., and Mulder, F.M. (2002). Equilibrium lithium transport between nanocrystalline phases in intercalated TiO2 anatase. Nature *418*, 397–399.

35. Ganapathy, S., Vanâ, Kentgens, A.P.M., Mulder, F.M., and Wagemaker, M. (2011). Equilibrium lithium-ion transport between nanocrystalline lithium-inserted anatase TiO_2 and the electrolyte. Chem. - A Eur. J. *17*, 14811–14816.

36. Yu, C., Ganapathy, S., Eck, E.R.H.V., Wang, H., Basak, S., Li, Z., and

Wagemaker, M. (2017). Accessing the bottleneck in all-solid state batteries, lithium-ion transport over the solid-electrolyte-electrode interface. Nat. Commun. *8*, 1–9.

37. Liu, Y., Li, B., Kitaura, H., Zhang, X., Han, M., He, P., and Zhou, H. (2015). Fabrication and performance of all-solid-state Li-Air battery with SWCNTs/LAGP cathode. ACS Appl. Mater. Interfaces *7*, 17307–17310.

38. Feng, J.K., Lu, L., and Lai, M.O. (2010). Lithium storage capability of lithium ion conductor $Li_{1.5}Al_{0.5}Ge_{1.5}(PO_4)_3$. J. Alloys Compd. *501*, 255–258.

39. Li, W.-D., Xu, C.-Y., Du, Y., Fang, H.-T., Feng, Y.-J., and Zhen, L. (2013). Electrochemical Lithium Insertion Behavior of -$Li_xV_2O_5$ ($0 \leqslant x \leqslant 3$) as the Cathode Material for Secondary Lithium Batteries. J. Electrochem. Soc. *161*, A75–A83.

40. Galy, J. (1992). Vanadium Pentoxide and Vanadium Oxide Bronzes-Structural Chemistry of SIngle (S) and Double (D) Layer $M_xV_2O_5$ Phases. J. Solid State Chem. *100*, 229–245.

41. Cocciantelli, J.M., Suh, K.S., Gas, J.N.I., Doumerc, J.P., and Soubeyroux, J.L. (1992). ^{7}Li NMR In electrochemically interfacalated γ-$Li_xV_2O_5$ bronzes ($0.95 \leqslant x \leqslant 1.9$). J. Phys. Chem. Solids *53*, 51–55.

42. Nishioka, D., Nakamura, K., Michihiro, Y., Ohno, T., Vijayakumar, M., Selvasekarapandian, S., and Deguchi, H. (2008). NMR study on Li^+ Ionic motion in $Li_xV_2O_5$ ($0.4 \leqslant x \leqslant 1.4$). J. Phys. Soc. Japan *77*, 024602.

43. Grey, C.P., and Dupre, N. (2004). NMR Studies of cathode materials for lithium-Ion rechargeable batteries. Chem. Rev. *104*, 4493–4512.

44. Vijayakumar, M., Selvasekarapandian, S., Nakamura, K., Kanashiro, T., and Kesavamoorthy, R. (2004). ^{7}Li MAS-NMR and vibrational spectroscopic investigations of $Li_xV_2O_5$($x=1.0$, 1.2 and 1.4). Solid State Ionics *167*, 41–47.

45. Stallworth, P.E., Johnson, F.S., Greenbaum, S.G., Passerini, S., Flowers, J., and Smyrl, W. (2002). Magnetic resonance studies of chemically intercalated $Li_xV_2O_5$ aerogels. J. Appl. Phys. *92*, 3839–3852.

46. Wagemaker, M., Krol, R. Van De, Kentgens, A.P.M., Well, A.A. Van, and Mulder, F.M. (2001). Two phase morphology limits lithium diffusion in TiO_2 (Anatase): A ^{7} Li MAS NMR Study. J. Am. Chem. Soc. *2*, 11454–11461.

47. Cocciantelli, J.M., Suh, K.S., Senegas, J., Doumerc, J.P., and Pouchard, M.

(1992). 7Li NMR of electrochemically inserted $Li_xV_2O_5$. J. Phys. Chem. Solids *53*, 57–59.

48. Liu, H., Choe, M.J., Enrique, R.A., Orvañanos, B., Zhou, L., Liu, T., Thornton, K., and Grey, C.P. (2017). Effects of antisite defects on Li diffusion in $LiFePO_4$ revealed by Li isotope exchange. J. Phys. Chem. C *121*, 12025–12036.

49. Famprikis, T., Canepa, P., Dawson, J.A., Islam, M.S., and Masquelier, C. (2019). Fundamentals of inorganic solid-state electrolytes for batteries. Nat. Mater. *18*, 1278-1291.

50. Hayamizu, K., and Seki, S. (2017). Long-range Li ion diffusion in NASICON-type $Li_{1.5}Al_{0.5}Ge_{1.5}(PO_4)_3$ (LAGP) studied by ^{7}Li pulsed-gradient spin-echo NMR. Phys. Chem. Chem. Phys. *19*, 23483–23491.

51. Doyle, M., and Newman, J. (1997). Analysis of capacity-rate data for lithium batteries using simplified models of the discharge process. J. Appl. Electrochem. *27*, 846–856.

52. Guo, P., Song, H., and Chen, X. (2009). Electrochemical performance of graphene nanosheets as anode material for lithium-ion batteries. Electrochem. commun. *11*, 1320–1324.

53. de Klerk, N.J.J., and Wagemaker, M. (2018). Space-Charge layers in all-solid-state batteries; Important or Negligible? ACS Appl. Energy Mater. *1*, 5609–5618.

54. Maier, J. (2005). Chemical potential of charge carriers in solids. Zeitschrift fur Phys. Chemie *219*, 35–46.

55. Hainovsky, N., and Maier, J. (1995). Simple phenomenological approach to premelting and sublattice melting in Frenkel disordered ionic crystals. Phys. Rev. B *51*, 15789–15797.

56. Swift, M.W., and Qi, Y. (2019). First-Principles prediction of potentials and space-charge layers in all-solid-state batteries. Phys. Rev. Lett. *122*, 167701.

57. Li, Z.Y., and Wu, Q.H. (2008). Electronic structures of $Li_xV_2O_5$ (x=0.5 and 1): A theoretical study. ChemPhysChem *9*, 300–304.

58. Schwietert, T.K., Arszelewska, V.A., Wang, C., Yu, C., Vasileiadis, A., de Klerk, N.J.J., Hageman, J., Hupfer, T., Kerkamm, I., Xu, Y., et al. (2020). Clarifying the relationship between redox activity and electrochemical stability in solid electrolytes. Nat. Mater. 19, 428-435.

59. Milewska, A., Ś, K., Tobola, J., Boudoire, F., Hu, Y., Bora, D.K., Mun, B.S., Braun, A., and Molenda, J. (2014). The nature of the nonmetal – metal transition in Li_xCoO_2 oxide . *263*, 110–118.

60. Horvai, G. (1991). Relationship between charge transfer resistance and exchange current density of ion transfer at the interface of two immiscible electrolyte solutions. Electroanalysis *3*, 673–675.

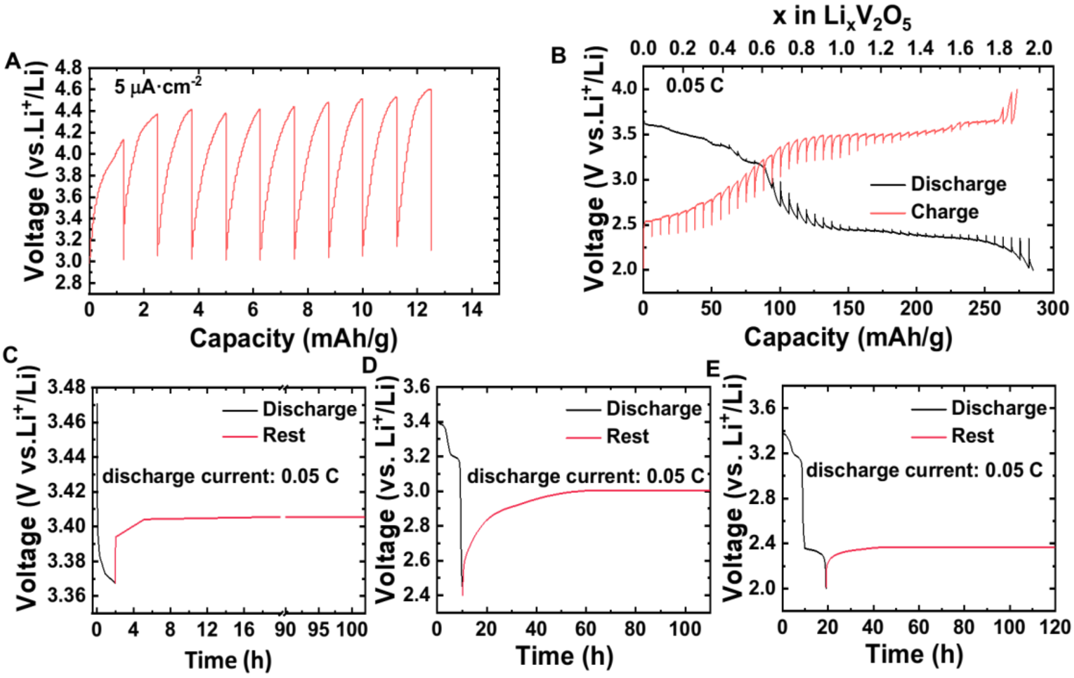

Figure 1. Determination of equilibrium potential of LAGP and $Li_xV_2O_5$ by GITT measurements. Both GITT measurements were set as charging/discharging for 30 mins and 8 h rest. The LAGP/Li cell was charged at a current density of 5 μA·cm^2. The V_2O_5/Li cell was charged/discharged at 0.05 C.

(A) GITT measurements of LAGP/Li cells.

(B) GITT measurements of V_2O_5/Li cells.

(C-E) Discharging V_2O_5/Li cell at 0.05 C for (C) 2 h, (D) 10h and (E) 20 h respectively then resting it for 100 h.

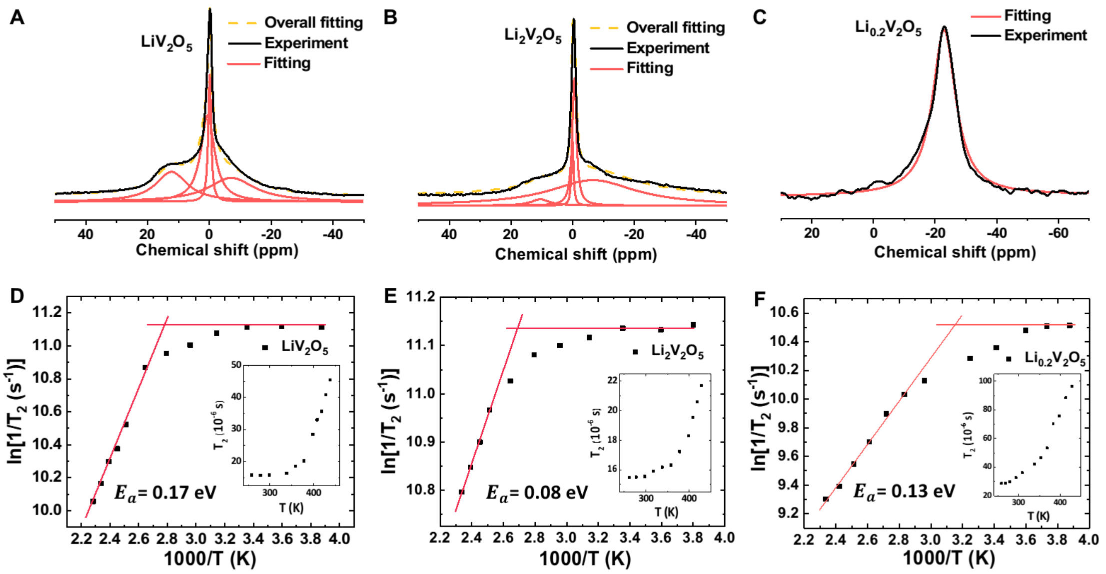

Figure 2. One dimensional (1D) NMR characterizations of LiV_2O_5, $Li_2V_2O_5$ and $Li_{0.2}V_2O_5$

(A-C) 1D ^{6}Li NMR spectrum of (A) LiV_2O_5, (B) $Li_2V_2O_5$ and (C) $Li_{0.2}V_2O_5$.

(D-E) Arrhenius plot of the ^{7}Li spin-spin relaxation time T_2 for (D) LiV_2O_5, (E) $Li_2V_2O_5$ and (F) $Li_{0.2}V_2O_5$.

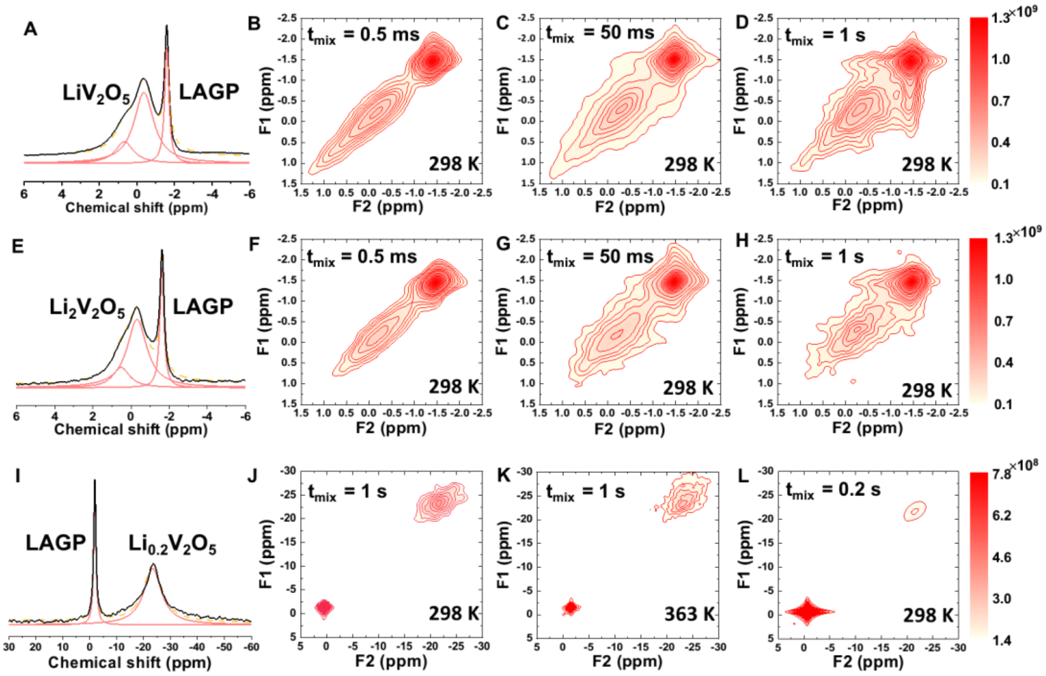

Figure 3. ^{6}Li NMR exchange experiments quantifying the spontaneous lithium-ion transport between the $Li_xV_2O_5$ and LAGP.

(A, E and I) 1D ^{6}Li MAS spectrum corresponding to (A) LiV_2O_5-LAGP, (E) $Li_2V_2O_5$-LAGP and (I) $Li_{0.2}V_2O_5$-LAGP.

(B-D) ^{6}Li 2D-EXSY spectrum of LiV_2O_5-LAGP at room temperature from short (0.5 ms) to long (1 s) mixing times.

(F-H) ^{6}Li 2D-EXSY spectrum of $Li_2V_2O_5$-LAGP at room temperature from short (0.5 ms) to long (1 s) mixing times.

(J) ^{6}Li 2D-EXSY spectrum of $Li_{0.2}V_2O_5$-LAGP at room temperature with 1 s mixing time.

(K) ^{6}Li 2D-EXSY spectrum of $Li_{0.2}V_2O_5$-LAGP at 363 K with 1 s mixing time.

(L) ^{7}Li 2D-EXSY spectrum of $Li_{0.2}V_2O_5$-LAGP at room temperature with 0.2 s mixing time.

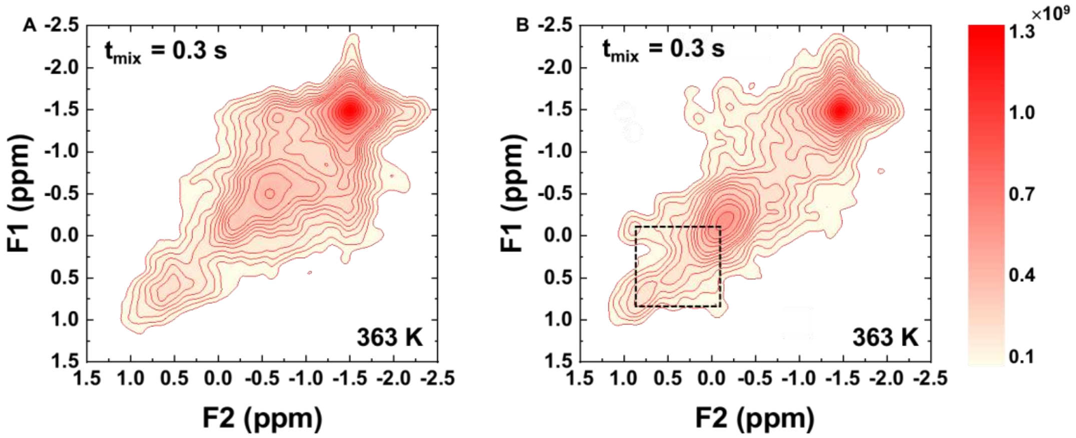

Figure 4. Exchange phenomenon within LiV_2O_5 and $Li_2V_2O_5$ bulk.

(A and B) ^{6}Li 2D exchange NMR spectrum of (A) LiV_2O_5-LAGP and (B) $Li_2V_2O_5$-LAGP at 363 K with 0.3 s mixing time.

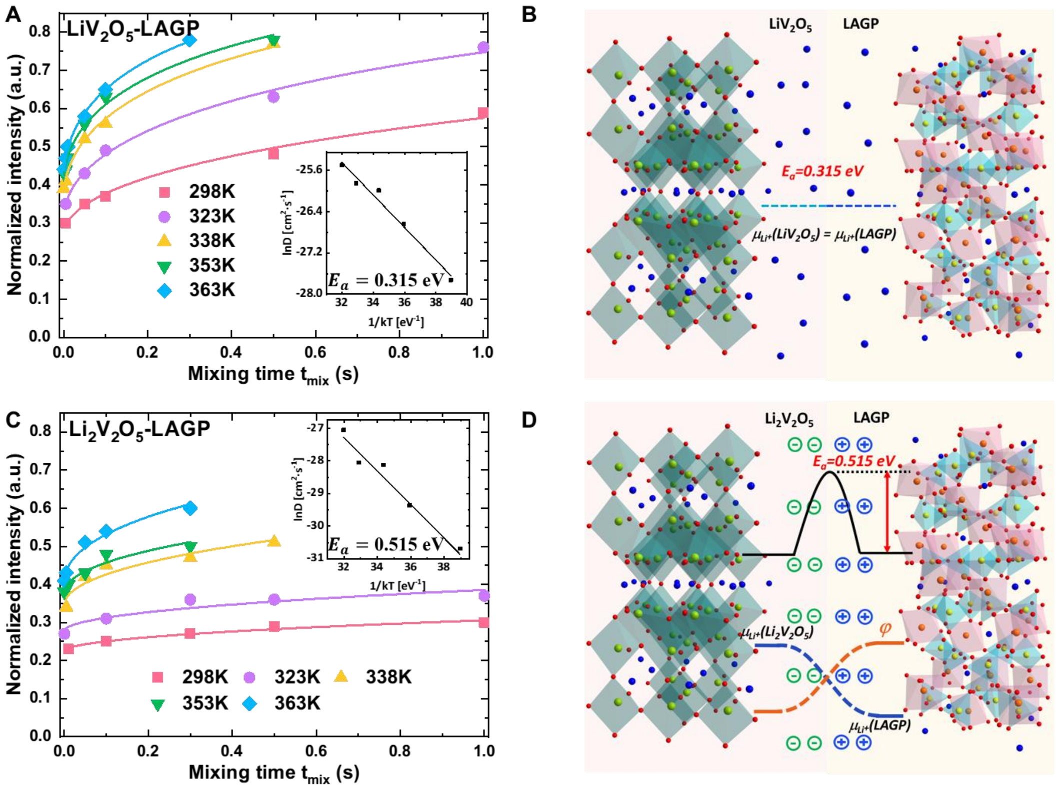

Figure 5. Determination of the activation energy of Li-ion exchange and schematic of space-charge layer effects on Li-ion transport.

(A and C) Normalized intensity of the cross-peaks in ^{6}Li exchange NMR spectrum as a function of mixing time at different temperatures for (A) LiV$_2$O$_5$-LAGP and (C) Li$_2$V$_2$O$_5$-LAGP. The insets show the temperature dependence of the diffusion parameters D based on the Arrhenius law.

(B and D) Schematic representation of the impact of the space-charge layer at the interface of (B) LiV$_2$O$_5$-LAGP and (D) Li$_2$V$_2$O$_5$-LAGP. The blue atoms represent the lithium-ion.

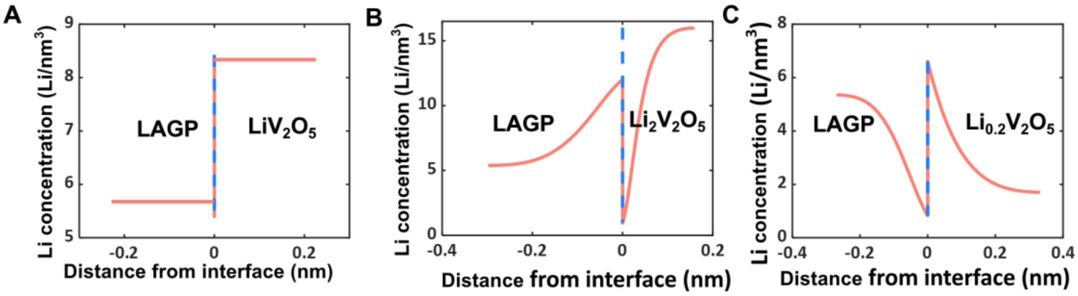

Figure 6. Space-charge layer model calculation of LiV_2O_5-LAGP, $Li_2V_2O_5$-LAGP and LiV_2O_5-LAGP interfaces.

(A-C) Lithium concentration at the (A) LiV_2O_5-LAGP interface, (B) $Li_2V_2O_5$-LAGP interface and (C) $Li_{0.2}V_2O_5$-LAGP interface.

Supplemental Information

Contents

1. Supplemental Figures and Tables

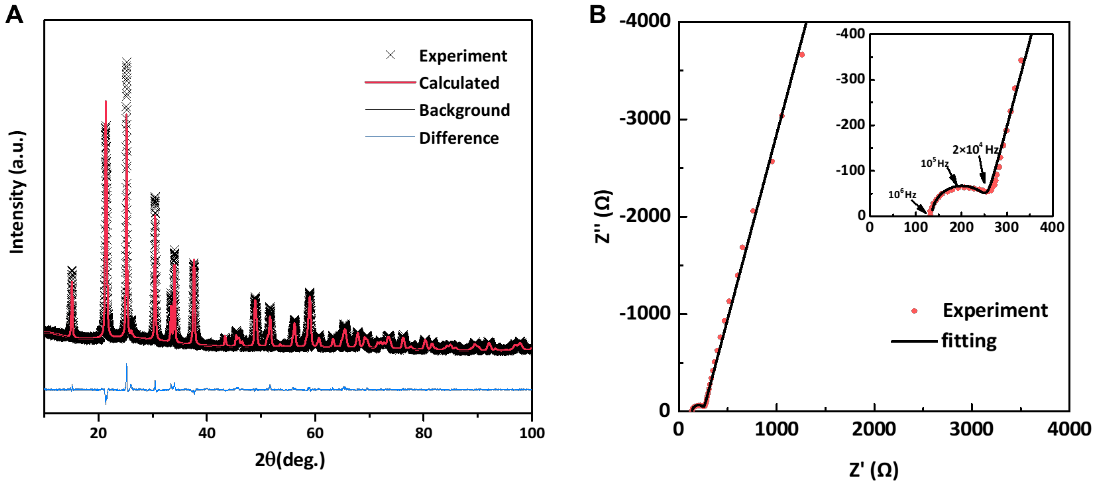

Figure S1. (A) XRD and Rietveld refinement of LAGP; (B) EIS curve of LAGP. The average crystallite size of LAGP is 110 nm obtained from the refinement result.

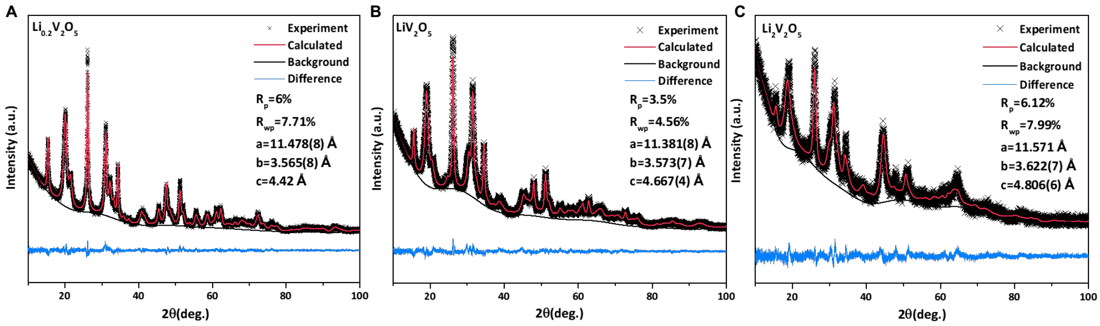

Figure S2. XRD and Rietveld refinements of (A)$Li_{0.2}V_2O_5$, (B)LiV_2O_5 and (C)$Li_2V_2O_5$. The average crystallite size of $Li_{0.2}V_2O_5$, LiV_2O_5 and $Li_2V_2O_5$ is 20 nm obtained from the refinement results.

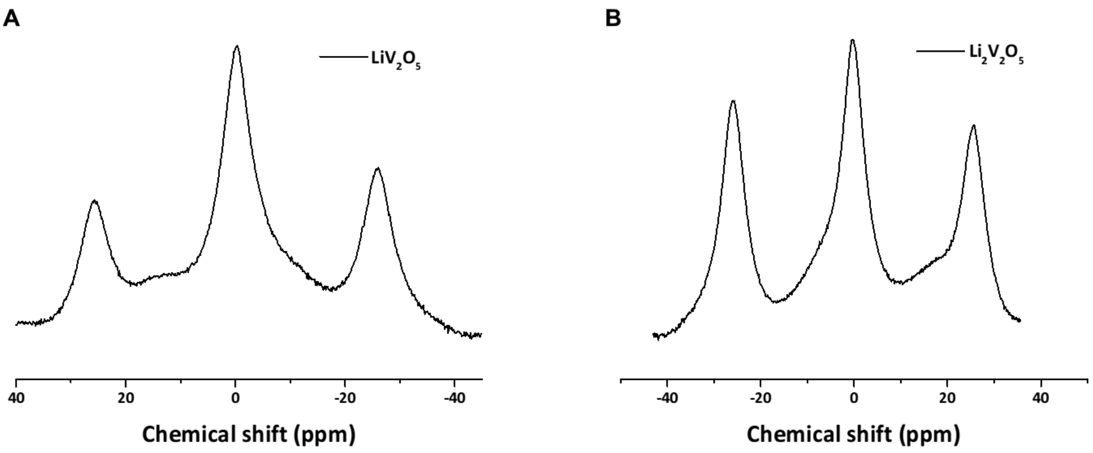

Figure S3. 1D ^{7}Li NMR spectrum of (A) LiV_2O_5 and (B) $Li_2V_2O_5$. In both spectrum the two resonances near 0 ppm overlap each other due to the strong dipolar interactions and quadrupolar interactions.

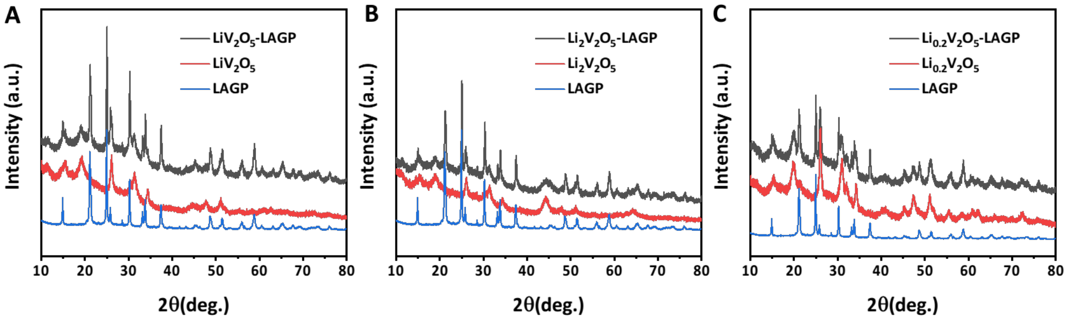

Figure S4. (A) XRD of LAGP, LiV_2O_5 and LiV_2O_5-LAGP. (B) XRD of LAGP, $Li_2V_2O_5$ and $Li_2V_2O_5$-LAGP (C) XRD of LAGP, $Li_{0.2}V_2O_5$ and $Li_{0.2}V_2O_5$-LAGP. All the XRD measurements were conducted 3 days after the $Li_xV_2O_5$ and LAGP mixing.

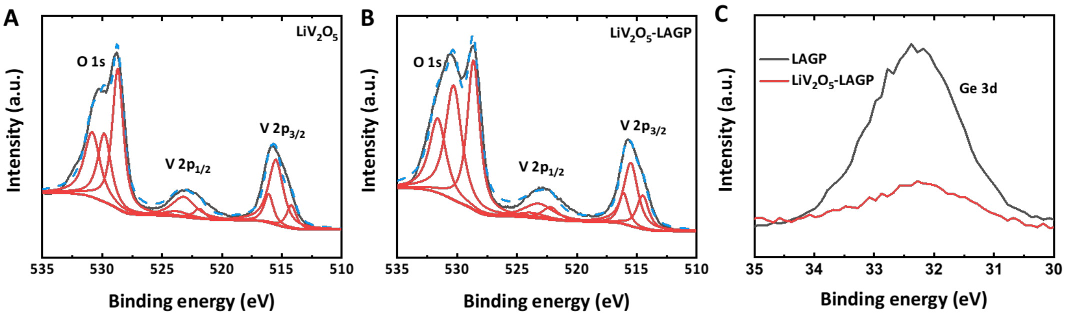

Figure S5. O 1s and V 2p XPS spectra of (A) LiV_2O_5 and (B) LiV_2O_5-LAGP. (C) Ge 3d XPS spectra of LAGP and LiV_2O_5-LAGP. The XPS results indicate the LiV_2O_5 and LAGP is stable against each other.

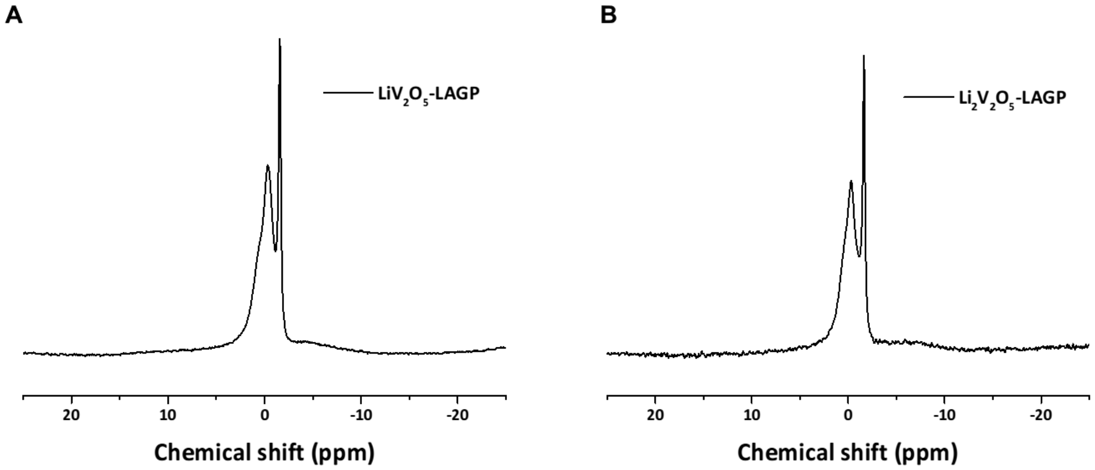

Figure S6. 1D ^{6}Li NMR spectrum of (A) LiV_2O_5-LAGP and (B) $Li_2V_2O_5$-LAGP. In both spectrum the two broad resonances locating at ~11 ppm and -8 ppm of LiV_2O_5 ($Li_2V_2O_5$) disappear due to the low intensity.

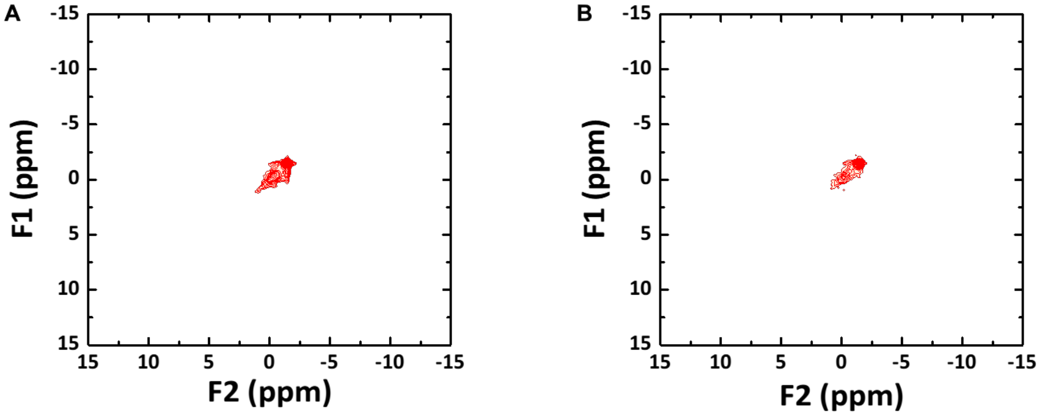

Figure S7. 2D ^{6}Li-^{6}Li exchange NMR spectrum of (A) LiV_2O_5-LAGP and (B) $Li_2V_2O_5$-LAGP. In both spectrum the two broad resonances locating at ~11 ppm and -8 ppm of LiV_2O_5 ($Li_2V_2O_5$) disappear due to the low intensity.

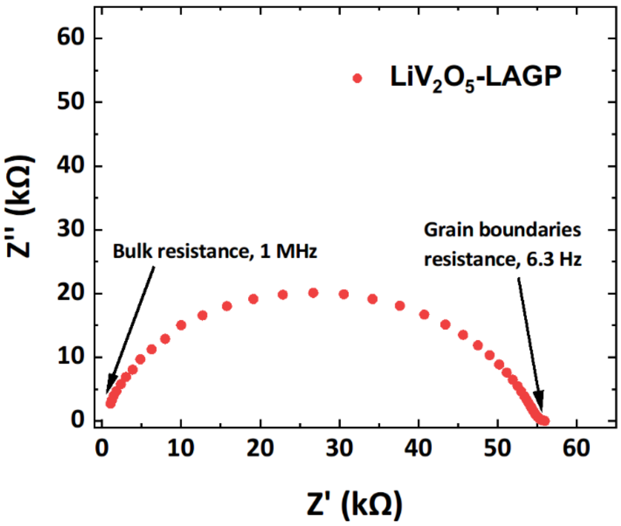

Figure S8. EIS measurement of LiV$_2$O$_5$-LAGP mixture. The diameter of the pellet is 8 mm and the thickness is 2 mm.

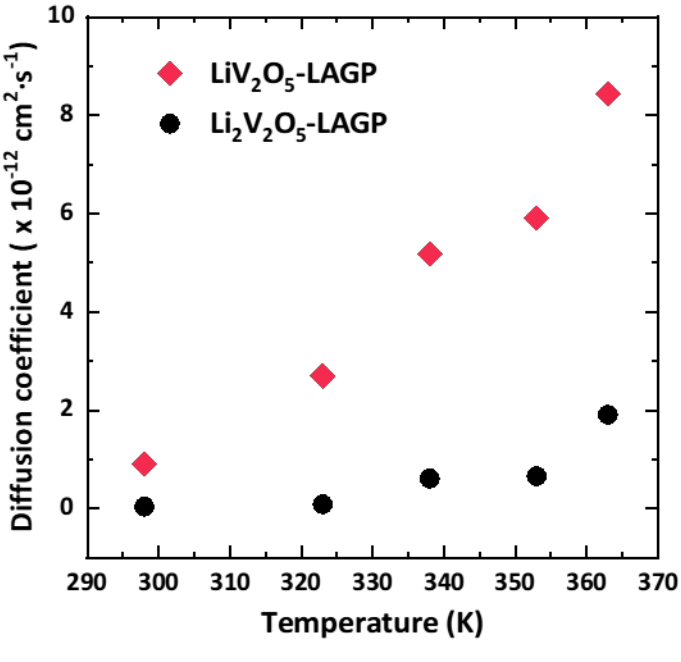

Figure S9. The diffusion coefficient of exchange lithium-ion at variable temperatures for LiV$_2$O$_5$-LAGP and Li$_2$V$_2$O$_5$-LAGP. At all measured temperature the diffusion coefficient of LiV$_2$O$_5$-LAGP is higher than that of Li$_2$V$_2$O$_5$-LAGP.

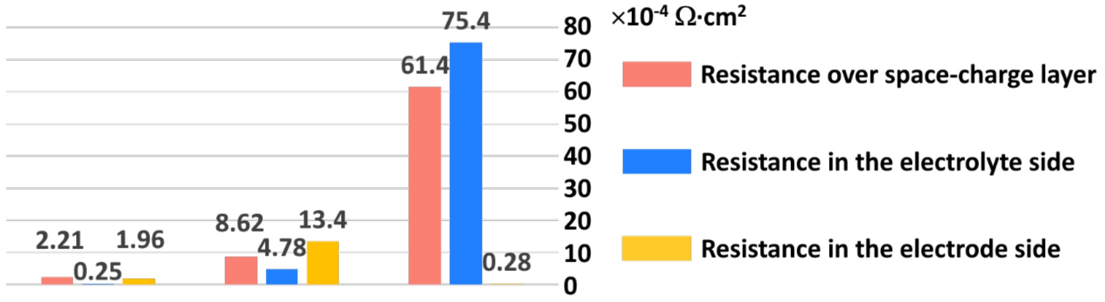

Figure S10. Calculated space-charge layer resistance at LiV_2O_5-LAGP, $Li_2V_2O_5$-LAGP and $Li_{0.2}V_2O_5$-LAGP interface.

Table S1 ICP result of the prepared $Li_xV_2O_5$ from chemical lithiation.

	Li(wt%)	V(wt%)	Li(mol)	V(mol)
$Li_{0.2}V_2O_5$	0.7	51.1	0.2	2.0
LiV_2O_5	3.2	50.8	1.1	2.0
$Li_2V_2O_5$	6.2	47.6	1.9	2.0

Table S2 Material properties used in the space-charge layer model.

Property	**LVO**	**LAGP**
C_{max} (Li/nm^3)	16.856[1]	13.06[2]
C_0 (Li/nm^3)	variable	5.37[2]
Voltage (vs Li$^+$/Li)	2.4~3.6 V	3 V
ε (relative to ε_0)	16.73[3]	41[4]
Ω (eV)	0.016[5]	0.0
E_M (eV/Li)	2.4[6]	4.7[7]
D* (cm^2/s)	$2*10^{-9}$[8]	10^{-9}[9]
D_{min} (cm^2/s)	$8*10^{-14}$[8]	-

2. Supplemental Experimental Procedures

Preparation of $Li_{0.2}V_2O_5$, LiV_2O_5, $Li_2V_2O_5$ and LAGP.

Nanosized V_2O_5 (JOHNSON MATTHEY, LONDON) were prepared by ball milling in ZrO_2 jar at 500 rpm for 4 h. The chemical lithiation of nanosized V_2O_5 was carried out by reaction with n-butyllithium(Aldrich, 1.6 M in hexane). The V_2O_5 powder was mixed with hexane (95+%, Aldrich), and the n-butyllithium was added while stirring the mixture. By adding different amount of n-butyllithium $Li_{0.2}V_2O_5$, LiV_2O_5 and $Li_2V_2O_5$ were prepared, during which process the color of the mixture changed from orange to dark green then to black, indicating that all the lithium successfully inserted into V_2O_5. After 3 days occasionally stirring, the samples were washed with hexane for 3 times then dried overnight in vacuum oven at 80 °C. The chemical lithiation process was carried out in an argon atmosphere glovebox to prevent reactions with oxygen and moisture. After preparation, the samples were analyzed for the Li/V ratio by atomic absorption/ICP analysis which confirmed that during preparation all the lithium reacted with the V_2O_5, thus yielding the overall compositions as mentioned, as shown in Table S1. The solid electrolyte LAGP was synthesized by a conventional solid-state reaction method. The starting materials Li_2CO_3 (99%, Alfa Aesar), Al_2O_3 (AR, Nanjing Chemical Reagent Co. P. R. China), GeO_2 (99.999%, Sinopharm Chemical Reagent Beijing Co., P. R. China) and $NH_4H_2PO_4$ (99%, Aladdin) were first ball milled in ZrO_2 jar at 400 rpm for 4 h. Then the mixture was sintered at 600 °C for 1 h and 900 °C for 6 h, respectively. After each sintering process the same ball milling process was carried out. After heat treatment at 900 °C, 0.75 g LAGP powder was pressed into a pellet using a 19 mm diameter die and annealed at 900 °C for 6 h for impedance measurement. For the 2D exchange experiments, LAGP and $Li_xV_2O_5$ powders were ballmilled at 600 rpm for 4 h separately first. The ballmilled $Li_xV_2O_5$ and LAGP powders were then mixed by hand grinding in a mortar for 30 mins to ensure they were mixed well. Then the mixture was pressed into a pellet with a hydraulic press under 100 MPa. After this the pellet was grinded in mortar to powder again for another 30 mins. Afterwards the powder mixture was well packed into the NMR rotor to ensure the steady MAS spinning at 8 kHz.

Cell assembly and electrochemical measurements

V_2O_5 and LAGP electrodes were prepared by mixing with carbon black, polyvinylidene fluorine (PVDF) with a mass ratio of 8:1:1 individually. Then the mixture was added to N-methyl pyrrolidone (NMP) solution and stirred for 6 h. The slurry was coated onto aluminum foil with doctor-blade and dried at 80 °C overnight. For the V_2O_5 /Li and LAGP/Li cell measurements, 2032-type coin cells were assembled with glass fiber separator, Li foil disk anode and 1 M $LiPF_6$ in EC/DMC electrolyte. GITT measurements of V_2O_5/Li and LAGP/Li cells were carried out in Maccor battery test equipment (series 4000).

Impedance spectroscopy, XRD and XPS characterization

Alternating-current (AC) impedance measurement was carried out on an impedance analyzer (Solartron 1287 coupled with Solartron 1260). The perturbation voltage of 5 mV in the frequency range of 1 MHz to 0.1 Hz was applied. Powder X-ray diffraction (XRD) patterns were collected over a two-theta range of 10-100° to identify the crystalline phases of the prepared materials using $Cu_{K\alpha}$ X-rays (1.5406 Å at 45 kV and 40 mA) on an X'Pert Pro X-ray diffractometer (PANalytical). A X-ray photoelectron spectrometer with Ar^+ beam was employed to investigate the element states in the samples (PHI5000 VersaProbe-II). Samples were placed on the XPS vacuum holder in the glove box and transferred to the XPS spectrometer to prevent moisture/air exposure.

Solid-state NMR measurement

^{6}Li (I=1/2, 92.6% abundance) NMR spectra were recorded on an Ascend 500 MHz Bruker spectrometer. The operating frequencies for ^{6}Li is 73.60 MHz and the spinning speed was set to 8 kHz. The chemical shift of ^{6}Li spectra were referenced with respect to 0.1 M LiCl solution. Single-pulse 1D spectra were recorded after a 90° radio frequency pulse of approximately 4 μs applied with a recycle delay of 10 s to ensure quantitative measurement conditions. Variable temperature two-dimensional (2D) exchange measurements were performed using a 4 mm MAS probe from 273 to 363 K. All 2D spectra consist of 8 scans for each of the 500 transients, each transient incremented by 200 μs with a recycle delay of up to 10 s. T_2 relaxation times were measured via a Hahn echo sequence (π/2 - τ - π - τ - acq) for a range of temperatures (258-438 K).

Spin-spin (T_2) relaxation model fitting

An often-applied model for the spin-spin relaxation due to fluctuations in the dipolar interactions caused by diffusion is the Bloembergen, Purcell, and Pound (BPP) model[10]. The BPP model for T_2 relaxation yields

$$1/T_2 = C_{dipole}\left\{\frac{3}{2}\tau_c + \frac{5}{2}\frac{\tau_c}{(1+\omega_0^2\tau_c^2)} + \frac{\tau_c}{(1+4\omega_0^2\tau_c^2)}\right\}$$

Where C_{dipole} is proportional to the rigid lattice second moment $\langle \Delta w^2 \rangle$. τ_c is the correlation time defining the time between lithium-ion hops, and ω_0 is the Larmor frequency. Between regime of rapid motion where $\langle \Delta w^2 \rangle^{1/2}\tau_c \ll 1$ and regime of slow motion where $\langle \Delta w^2 \rangle^{1/2}\tau_c \gg 1$, a break point occurs where $\tau_c = T_2/\sqrt{2}$. Assuming the mobility of the ions to be thermally activated, the correlation time will obey an Arrhenius law, $\tau_c = \tau_\infty \exp(E_a/k_B T)$, where E_a is the activation energy of the jump process, and $1/\tau_\infty$ is the attempt frequency. For large T_2, the correlation times obey $\langle \Delta w^2 \rangle^{1/2} \tau_c \ll 1$, but still $\omega_0 \tau_c > 1$, which means that within the BPP model, $1/T_2 = 3\tau_c\, C_{dipole}/2 \propto \tau_\infty \exp(E_a/k_B T)$. As a result, an Arrhenius plot of $\ln(1/T_2)$ versus $1/T$ in this range leads to a determination of the activation energy.

Quantification of interfacial exchange

Quantification of exchange between the LiV_2O_5 ($Li_2V_2O_5$) and LAGP was performed by fitting the growing off-diagonal signal to a diffusion model where in a solution to Fick's law for diffusion is determined $\frac{\partial m(\vec{r},\vec{t})}{\partial t} = \vec{\nabla} \cdot \{D(\vec{r}) m(\vec{r},\vec{t})\}$, where $m(\vec{r},\vec{t})$ is the magnetization of Li at position $\vec{r}$ and t and D is the lithium-ion self-diffusion coefficient. By using the mathematical models of Schmidt-Rohr and co-workers for spin diffusion, and by assuming the overall diffusivity to be equal to the effective diffusion coefficient, the rate of demagnetization of lithium ions in the LAGP can be set equal to the initial magnetization minus the rate of magnetization in the LiV_2O_5 ($Li_2V_2O_5$). Assuming a cubic shaped LAGP phase embedded in an infinite LiV_2O_5 ($Li_2V_2O_5$) phase, this leads to the following analytical expression for the rate of demagnetization from the LAGP into LiV_2O_5 ($Li_2V_2O_5$) particles as

$$\mathrm{m}(t_{mix}) = \left\{ \frac{m_0}{2} \sqrt{4Dt_{mix}} \left[ierfc\left(\frac{d}{\sqrt{4Dt_{mix}}} \right) + ierfc\left(\frac{-d}{\sqrt{4Dt_{mix}}} \right) - \frac{2}{\sqrt{\pi}} \right] \right\}^3$$

where $\mathrm{ierfc(x)} = 1/\sqrt{\pi} \exp(-x^2) - x[l - \mathrm{erf}(x)]$ and d is the Li diffusion distance from the LAGP particle to the LiV_2O_5 ($Li_2V_2O_5$). Assuming that exchange on average occurs form the centre of a LAGP particle to the centre of the $Li_xV_2O_5$ particles, having individual particle sizes of 110 nm and 20 nm respectively, this leads to an average diffusion distance of 65 nm.

Space-charge layer model calculation

The space-charge model adopted here is from a previous paper of our group[11] where the detailed theories and model building processes are well described. The assumptions of this model include that the interface contact is perfect; $Li_xV_2O_5$ and LAGP are chemically stable to each other; only the lithium-ion is mobile at the interface. By using a solid solution model the chemical potential as a function of the distance near the interface can be determined from the corresponding ion concentration, where the law of mass conservation serves as the boundary condition. Specially the columbic interaction between defects is taken into consideration to get better approximation of the formation energy for the vacancies. The parameters of

$Li_xV_2O_5$ and LAGP used in this model are listed in Table S2. The formation energy of LAGP is unavailable, and therefore, the formation energy of another NASICON material $LiTi_2(PO_4)_3$ is used in this model as an approximation.

References

1. W., Wang, H., Liu, S., and Huang, J. (2012). Synthesis of γ-LiV2O5 nanorods as a high-performance cathode for Li ion battery. J. Solid State Electrochem. *16*, 2555–2561.

2. Weiss, M., Weber, D.A., Senyshyn, A., Janek, J., and Zeier, W.G. (2018). Correlating Transport and Structural Properties in Li1+ xAlxGe2- x(PO4)3 (LAGP) Prepared from Aqueous Solution. ACS Appl. Mater. Interfaces *10*, 10935–10944.

3. Popović, Z. V., Gajić, R., Konstantinović, M.J., Provoost, R., Moshchalkov, V. V., Vasil'ev, A.N., Isobe, M., and Ueda, Y. (2000). Infrared and Raman spectra of LiV2O5 single crystals. Phys. Rev. B *61*, 11454–11459.

4. Chung, H., and Kang, B. (2014). Increase in grain boundary ionic conductivity of Li1.5Al0.5Ge1.5(PO4)3 by adding excess lithium. Solid State Ionics *263*, 125–130.

5. Zhao, X., Zhang, X., Wu, D., Zhang, H., Ding, F., and Zhou, Z. (2016). Ab initio investigations on bulk and monolayer V2O5 as cathode materials for Li-, Na-, K- and Mg-ion batteries. J. Mater. Chem. A *4*, 16606–16611.

6. https://materialsproject.org/materials/mp-19408/

7. Chen, L.J., Zhao, Y.J., Luo, J.Y., and Xia, Y.Y. (2011). Oxygen vacancy in LiTiPO5 and LiTi2(PO 4)3: A first-principles study. Phys. Lett. Sect. A Gen. At. Solid State Phys. *375*, 934–938.

8. Li, W.-D., Xu, C.-Y., Du, Y., Fang, H.-T., Feng, Y.-J., and Zhen, L. (2013). Electrochemical Lithium Insertion Behavior of LixV2O5 (0<x≤3) as the Cathode Material for Secondary Lithium Batteries. J. Electrochem. Soc. *161*, A75–A83.

9. Hayamizu, K., and Seki, S. (2017). Long-range Li ion diffusion in NASICON-type Li1.5Al0.5Ge1.5(PO4)3 (LAGP) studied by 7 Li pulsed-gradient spin-echo NMR. Phys. Chem. Chem. Phys. *19*, 23483–23491.

10. Bloembergen, N., Purcell, E.M., and Pound, R. V. (1948). Relaxation effects in nuclear magnetic resonance absorption. Phys. Rev. *73*, 679–712.

11. de Klerk, N.J.J., and Wagemaker, M. (2018). Space-Charge Layers in All-Solid-State Batteries; Important or Negligible? ACS Appl. Energy Mater. *1*, 5609–5618.